Commensurate-incommensurate magnetic phase transitions of CePtAl

1995 J. Phys.: Condens. Matter 7 1663

(http://iopscience.iop.org/0953-8984/7/8/013)

J. Phys.: Condens. Matter 7 (1995) 1663–1678. Printed in the UK

Commensurate–incommensurate magnetic phase transitions of CePtAl

A Dönni†, H Kitazawa†, P Fischer‡, J Tang§, M Kohgi‖, Y Endoh‖ and Y Morii¶

† The Institute of Physical and Chemical Research (RIKEN), Wako, Saitama 351-01, Japan
‡ Laboratory for Neutron Scattering, ETH Zürich, and Paul Scherrer Institute, CH-5232 Villigen PSI, Switzerland
§ National Research Institute for Metals, Tsukuba, Ibaraki 305, Japan
‖ Department of Physics, Faculty of Science, Tohoku University, Sendai 980, Japan
¶ Neutron Scattering Laboratory, Japan Atomic Energy Research Institute (JAERI), Tokai, Ibaraki 319-11, Japan

Received 5 July 1994, in final form 26 September 1994

Abstract. The magnetic properties of CePtAl with orthorhombic TiNiSi-type chemical structure were investigated. Single-crystal experiments of electrical resistivity, specific heat and magnetic susceptibility reveal the existence of three magnetic phase transitions at $T_1 = 5.9$ K (second order), $T_2 = 4.3$ K (first order) and $T_3 = 2.2$ K (first order). Powder neutron diffraction measurements detected complex magnetic structures consisting of two coexisting, partly incommensurate magnetic propagation vectors: $k_1 = 0$ and $k_3 = [0, 0.463(8), 0]$ for $T_2 \leqslant T \leqslant T_1$; and $k_1 = 0$ and $k_2 = [0, 1/2, 0]$ for $T \leqslant T_2$. The predominantly ferromagnetic k_1 component and the antiferromagnetic k_2 component of the magnetic low-temperature structure of CePtAl were refined at 1.5 K. Magnetism in CePtAl is dominated by a ferromagnetic component $(1.35(4)\mu_B$ at 1.5 K) oriented parallel to the magnetically easy a axis. The complexity of magnetic structures in CePtAl appears to be caused by competing anisotropic magnetic exchange interactions in a network, where Ce–Ce nearest neighbours (3.56 Å) form chains parallel to the b axis and Ce–Ce second-nearest neighbours (3.77 Å) form chains along the a axis.

1. Introduction

Investigations of ternary rare-earth intermetallic compounds continue to be an active topic of research because of their intriguing magnetic properties. One aspect is geometrical frustration. In the antiferromagnetic compound TbNiAl [1] with hexagonal ZrNiAl-type chemical structure, the magnetic Tb atoms have triangular coordination symmetry. In such a triangle, two nearest neighbours to a given Tb atom are themselves nearest neighbours and antiferromagnetic coupling among them cannot be completely satisfied. The result for TbNiAl is a complex magnetic phase diagram with several phase transitions. Below $T_N = 44.6$ K the magnetic structure of TbNiAl has been described [1] by the magnetic propagation vectors $k_1 = [1/2, 0, 1/2]$ and $k_2 = [1/2, 1/2, 1/2]$. At a second phase transition at $T_1 = 23.5$ K the frustrated Tb spins change directions and/or the magnitudes of the ordered moments. For CePtAl the origin of frustration (competing magnetic exchange interactions between Ce–Ce nearest neighbours and Ce–Ce second-nearest neighbours) is different from TbNiAl, but the resulting complexity of magnetic structures and phase transitions in CePtAl (reported in the present paper) is found to be comparable to the case of TbNiAl.

0953-8984/95/081663+16$19.50

Crystallographic studies of CePtAl have been reported only very recently [2–4]. CePtAl was found [2] to crystallize in the orthorhombic TiNiSi-type structure (space group *Pnma*) with room-temperature lattice parameters $a = 7.1998(6)$ Å, $b = 4.4817(4)$ Å and $c = 7.7938(5)$ Å. The TiNiSi-type structure is adopted by all rare-earth platinum aluminides LnPtAl (Ln = La, Ce, Pr, Nd, Sm, Gd, Tb, Dy, Ho, Er, Tm, Lu). For the LnPtAl phases the lanthanide contraction results in a decrease of the room-temperature lattice parameters a, b and c with increasing atomic number. Both a and b show a linear dependence on the rare-earth radii, whereas c displays a non-linear behaviour. A weak anomaly is observed for CePtAl. The a axis is slightly too large while the c axis is too short. The b axis and unit-cell volume, however, are quite normal.

First investigations of the physical properties of polycrystalline CePtAl samples were performed by Hulliger [2]. In the paramagnetic susceptibility of CePtAl no deviation from a Curie–Weiss law was detectable. The effective magnetic moment $\mu_{\text{eff}} = 2.47\mu_B$ is close to the free-ion value of $2.54\mu_B$ for the $^2F_{5/2}$ ground-state multiplet of Ce^{3+} ions. The positive value of the paramagnetic Curie temperature $\Theta_p = 7$ K indicates ferromagnetic interactions. Magnetic ordering occurs around 6 K. A spontaneous magnetization of $1.2\mu_B$ was measured on loose CePtAl powder at 2 K. The electrical resistivity [4] shows no evidence for a Kondo effect in CePtAl.

Experiments on CePtAl single crystals by Kitazawa [5] revealed a pronounced anisotropy of magnetic properties. In the paramagnetic susceptibility, considerable deviations from Curie–Weiss behaviour were observed for χ_b and χ_c (not for χ_a), which are probably due to crystalline electric field effects. For the magnetization of CePtAl at 5 K the highly anisotropic values of $m_a = 1.5\mu_B$, $m_b = 0.2\mu_B$ and $m_c = 0.1\mu_B$ were measured in a magnetic field of 5 T applied along a, b and c axes, respectively. For m_a the experiment yielded a spontaneous magnetic moment of $1.0\mu_B$ ($T = 5$ K) and a ferromagnetic zero-field saturation moment of $1.35\mu_B$ (obtained by an extrapolation from the almost linear behaviour of m_a between 2.5 T and 5 T to $H = 0$).

We have started a more detailed investigation of the nature of the magnetically ordered states in CePtAl. In the present work we report on single-crystal measurements of electrical resistivity, specific heat and magnetic susceptibility as well as on powder neutron diffraction experiments. The results show for the first time the existence of three magnetic phase transitions in CePtAl between 2.2 and 5.9 K. The magnetic structures turn out to be considerably more complicated than a simple ferromagnet and consist of two coexisting, partly incommensurate magnetic propagation vectors. The present neutron diffraction experiments provide an important first overview of the complex magnetic structures in CePtAl, including a determination of all magnetic propagation vectors and a refinement of the two Fourier components of the magnetic low-temperature ordering. But to establish the nature of coupling between the two magnetic propagation vectors, additional magnetic-field- or pressure-dependent single-crystal neutron experiments on CePtAl will be necessary.

2. Experimental details

Polycrystalline samples of CePtAl and of the non-magnetic reference compound LaPtAl were synthesized by arc-melting stoichiometric mixtures of the pure elements in an argon atmosphere. To improve homogeneity the samples were annealed at 900 °C for 5 days in high vacuum. CePtAl single crystals were grown by the Czochralski method from a stoichiometric melt. Room-temperature lattice parameters of the samples were determined by the x-ray whole powder pattern decomposition method [6]. The values obtained for

annealed polycrystalline CePtAl (a = 7.1980(4) Å, b = 4.4810(3) Å, c = 7.7956(4) Å) and for powdered single-crystalline CePtAl (a = 7.2006(5) Å, b = 4.4900(2) Å, c = 7.7789(4) Å) are consistent with the lattice parameters reported for several CePtAl samples [2–4]. Electrical resistivity measurements in the temperature range from 1.4 to 300 K were performed along a, b and c axes of a CePtAl single crystal by the conventional four-terminal DC method. The specific heat of CePtAl and LaPtAl was measured by the adiabatic technique. The magnetic susceptibility was measured in a field of 0.1 T applied parallel to the c axis of a CePtAl single crystal by using a SQUID (superconducting quantum interference device) magnetometer.

For the neutron diffraction experiments a large amount (21 g) of CePtAl powder was filled under a helium gas atmosphere into a cylindrical vanadium container of 10 mm diameter and 45 mm height and mounted in a standard ^{4}He ILL-type cryostat. Measurements at the 10 MW reactor Saphir at the Paul Scherrer Institute, Switzerland, were performed on the multicounter powder diffractometer DMC [7] with 400 detectors. The incident neutron wavelengths λ = 1.6984 Å (high-resolution mode) and 1.7037 Å (high-intensity mode), respectively, were obtained from a vertically focused germanium (3 1 1) monochromator. Cryostat peaks were suppressed by an oscillating radial collimator ($\alpha_3 \geqslant 12'$). The chemical structure of CePtAl was measured at 11 K in the paramagnetic state on DMC operated in the high-resolution mode (primary collimation $\alpha_1 = 10'$). Diffraction data were collected for 5 h per point in the angular range from 3° to 134.8° with steps $\Delta(2\theta) = 0.1°$. To determine the magnetic structure of CePtAl, further measurements were performed at 1.5 K and at 11 K on DMC operated in the high-intensity mode (primary collimator removed). Here diffraction patterns were recorded for 11 h per point and temperature in the angular range from 3° to 8.28° with steps $\Delta(2\theta) = 0.1°$. All intensities were corrected for absorption according to the measured transmission (μR = 0.115). Additional investigations of the temperature dependence of magnetic Bragg peaks of polycrystalline CePtAl were carried out in the temperature range from 1.5 to 11 K at the 20 MW reactor JRR3M at Tokai, Japan, on the triple-axis spectrometers TOPAN and TAS2, which were operated in the two-axis mode. A neutron wavelength λ = 2.337 Å and collimations in front of and behind the sample of 30′/30′ (TOPAN) and 40′/40′ (TAS2) were used. Higher-order contamination, with intensities comparable to the weak magnetic peak (1,0,0) of CePtAl, were eliminated by inserting a pyrolitic graphite filter into the incoming neutron beam.

3. Results and analysis

3.1. Magnetic phase transitions

The normalized electrical resistivity $\rho(T)/\rho(300\ \mathrm{K})$ measured parallel to a, b and c axes of a CePtAl single crystal is shown in figure 1(a). All three resistivity curves in figure 1(a) exhibit sharp steps at T_2 = 4.3 K and T_3 = 2.2 K, indicating first-order magnetic phase transitions. Measurements for increasing and decreasing temperature yield an upper limit of 0.1 K for hysteresis of the two phase transitions.

Specific-heat data measured on a CePtAl single crystal (figure 1(b)) reveal a second-order magnetic phase transition at T_1 = 5.9 K and first-order phase transitions at T_2 = 4.3 K and $T_3 \simeq$ 2.8 K. Above T_1 short-range magnetic correlations are present in CePtAl. The magnetic part of the specific heat, c_{mag}, was determined from the difference of specific heat of CePtAl and of the non-magnetic LaPtAl. The magnetic entropy S_{mag}, obtained by integrating c_{mag}/T up to the phase transition T_1, reaches 72% of the value $R \ln 2$, the entropy of the crystalline electric ground-state doublet of CePtAl.

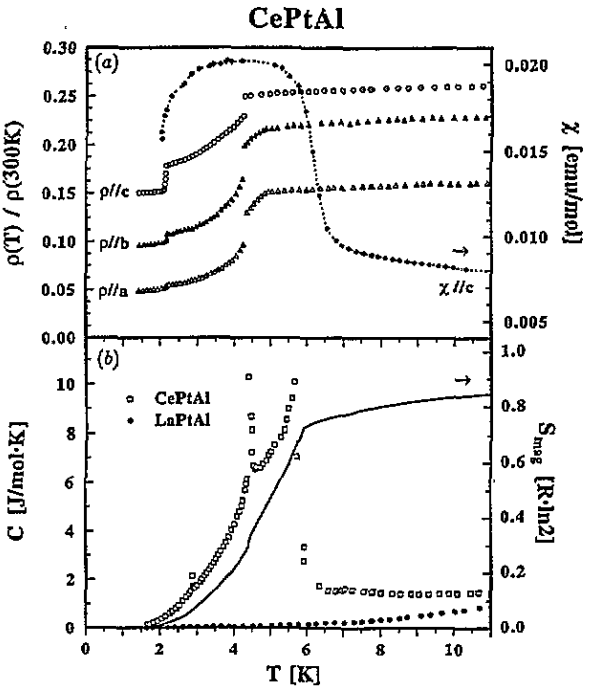

Figure 1. (*a*) Normalized electrical resistivity $\rho(T)/\rho(300\ \mathrm{K})$ versus T measured for increasing temperature parallel to a, b and c axes of a CePtAl single crystal (left-hand axis). The curves $\rho \parallel b$ and $\rho \parallel c$ have been shifted for clarity by 0.05 and 0.10, respectively. The room-temperature values $\rho(300\ \mathrm{K})$ are 104, 109 and 117 $\mu\Omega$ cm for $\rho \parallel a$, $\rho \parallel b$ and $\rho \parallel c$, respectively, with a systematic experimental error of about 15%. Also shown is the temperature dependence of magnetic susceptibility $\chi(T)$ measured in a field of 0.1 T applied parallel to the c axis of a CePtAl single crystal (right-hand axis). The broken curve is a guide to the eye. (*b*) Thermal variations of specific heat $C(T)$ of CePtAl and LaPtAl and of magnetic entropy S_{mag}. The magnetic contribution to S_{mag} below 1.65 K is neglected (estimated value $0.01R\ln 2$).

The magnetic susceptibility $\chi \parallel c$ of CePtAl (figure 1(*a*)) displays an anomaly, which corresponds to a pronounced increase and decrease in magnitude near the phase transitions $T_1 = 5.9$ K and $T_3 = 2.2$ K, respectively, and which is insensitive to the transition at $T_2 = 4.3$ K.

The different experiments; i.e. electrical resistivity, specific heat, magnetic susceptibility and powder neutron diffraction (section 3.4), yield consistent values for the phase transitions at $T_1 = 5.9$ K and $T_2 = 4.3$ K. The inconsistent values obtained for $T_3 = 2.2$ K may be due to limited experimental accuracy of measurements of small effects. The specific heat anomaly at $T_3 \simeq 2.8$ K consists of only one data point. The neutron experiment shows a change of intensity of a weak magnetic peak at $T_3 \simeq 2.5$ K. The most accurate measurement is certainly the pronounced step in the electrical resistivity curves at $T_3 = 2.2$ K. In addition, the presence of a slight sample dependence of the transition temperature T_3 cannot be ruled out.

3.2. Chemical structure of CePtAl at 11 K

The 11 K neutron diffraction pattern of paramagnetic CePtAl displayed in figure 2 corresponds well to the previously reported [2, 3] orthorhombic TiNiSi-type structure (space

group *Pnma* with all atoms in sites (4c)). A total of 191 inequivalent nuclear Bragg reflections were refined by a modified version of the Wiles–Young program [8], including a fit of the background represented by a self-adjusting polynomial. The resulting structural parameters for CePtAl at 11 K are listed in table 1. The refinement, based on the nuclear scattering lengths published by Sears [9], finally converged to the agreement values $R_{wp} = 5.5\%$ and $R_I = 4.3\%$ concerning weighted and integrated intensities, respectively. From counting statistics, the expected value is calculated to be $R_e = 2.3\%$, yielding $\chi^2 = (R_{wp}/R_e)^2 = 5.8$. The thermal expansion of CePtAl is anisotropic. Upon decreasing the temperature from 295 K to 11 K, the ratio of lattice parameters b/a remains constant, whereas the values c/a and c/b decrease by 1.1(2)%. The atomic positions of table 1 are consistent with the x-ray single-crystal structure results of CePtAl at room temperature [3] within typically 0.002.

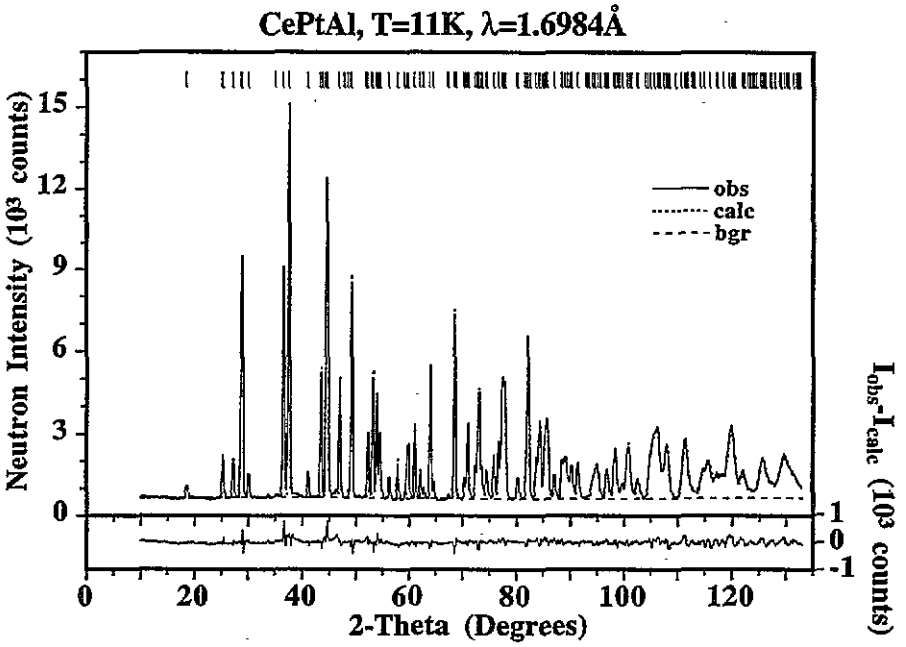

Figure 2. Observed, calculated and difference neutron diffraction patterns of paramagnetic CePtAl at $T = 11$ K (DMC, high-resolution mode, $\lambda = 1.6984$ Å). Peak positions are indicated by the vertical bars on top of the figure.

The crystal structure of CePtAl is shown in figure 3 as a view onto the (0, 1, 0) plane. The chemical unit cell contains four magnetic Ce atoms with positions Ce(1) at $(x, 1/4, z)$, Ce(2) at $(\bar{x} + 1/2, 3/4, z + 1/2)$, Ce(3) at $(\bar{x}, 3/4, \bar{z})$ and Ce(4) at $(x + 1/2, 1/4, \bar{z} + 1/2)$. Concerning interatomic Ce–Ce distances at 11 K, Ce(1) has two nearest neighbours Ce(3) at 3.578(1) Å, two second-nearest neighbours Ce(4) at 3.771(1) Å and two third-nearest neighbours Ce(1) at 4.489(1) Å. Thus the Ce–Ce distances for nearest neighbours and second-nearest neighbours are not very different and significantly shorter than for third-nearest neighbours. Nearest neighbours form infinite chains parallel to the b axis (Ce(1)–Ce(3)–Ce(1)... and Ce(2)–Ce(4)–Ce(2)... ..). Second-nearest neighbours form infinite chains parallel to the a axis (Ce(1)–Ce(4)–Ce(1)... and Ce(2)–Ce(3)–Ce(2)...). The angle Ce(4)–Ce(1)–Ce(1) amounts to $\alpha_N = 17.1° \pm 0.1°$ (see figure 3).

Table 1. Structural parameters of CePtAl at 11 K determined by neutron diffraction. Orthorhombic space group *Pnma* (No 62), Z = 4. The relative errors given in parentheses include estimated standard deviations of the fit. An additional systematic error due to uncertainty of neutron wavelength enlarges the errors of lattice parameters *a*, *b* and *c*, but does not affect atomic positions *x*/*a*, *y*/*b* and *z*/*c* and ratios of lattice parameters *b*/*a*, *c*/*a* and *c*/*b*.

(*a*) Lattice constants					
$a = 7.2084(7)$ Å		$b = 4.4891(4)$ Å		$c = 7.7190(8)$ Å	
(*b*) Atomic positions and isotropic temperature factors					
Atom	Site	*x*/*a*	*y*/*b*	*z*/*c*	*B* (Å^2)
Ce	(4c)	0.0305(3)	0.25	0.6782(3)	0.4(1)
Pt	(4c)	0.2861(1)	0.25	0.3872(1)	0.1(1)
Al	(4c)	0.1446(4)	0.25	0.0672(4)	0.3(1)

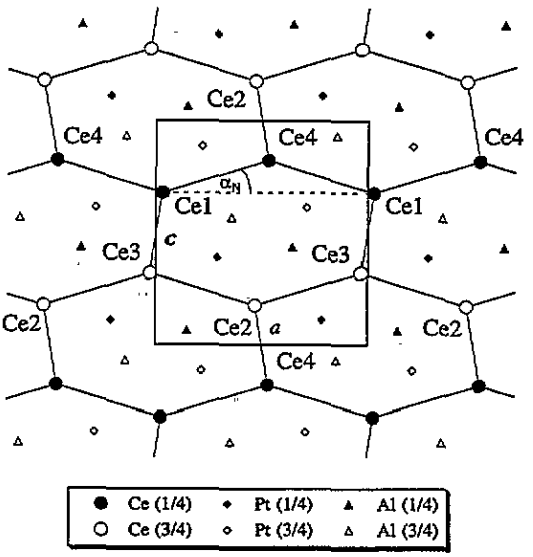

Figure 3. View onto the (0, 1, 0) plane of the nuclear structure of CePtAl. The heights of the atoms in units (*y*/*b*) are indicated by numbers in parentheses in the legend.

3.3. Magnetic structure of CePtAl at 1.5 K

To observe magnetic Bragg peaks of CePtAl, DMC measurements in the high-intensity mode were performed at 1.5 and 11 K. The difference neutron diffraction pattern $I(1.5\ \mathrm{K}) - I(11\ \mathrm{K})$ shown in figure 4 clearly reveals additional magnetic Bragg intensity.

For small 2θ values the difference pattern of figure 4 exhibits a negative background level, which reflects the change of background between the paramagnetic and magnetically ordered phase of CePtAl. At 11 K in the paramagnetic state the magnetic Ce moments are oriented randomly. Paramagnetic neutron scattering gives rise to an additional diffuse (incoherent) intensity contribution to the background, which diminishes with $\sin\theta/\lambda$ (θ = scattering angle, λ = neutron wavelength) proportional to the square of the neutron magnetic form factor of Ce^{3+}. With increasing 2θ value the background of figure 4 increases monotonically from the negative value of about -1000 counts at $2\theta = 3°$ to (within experimental error) 0 counts at around $2\theta = 75°$. At $2\theta = 8.0°$ the observed

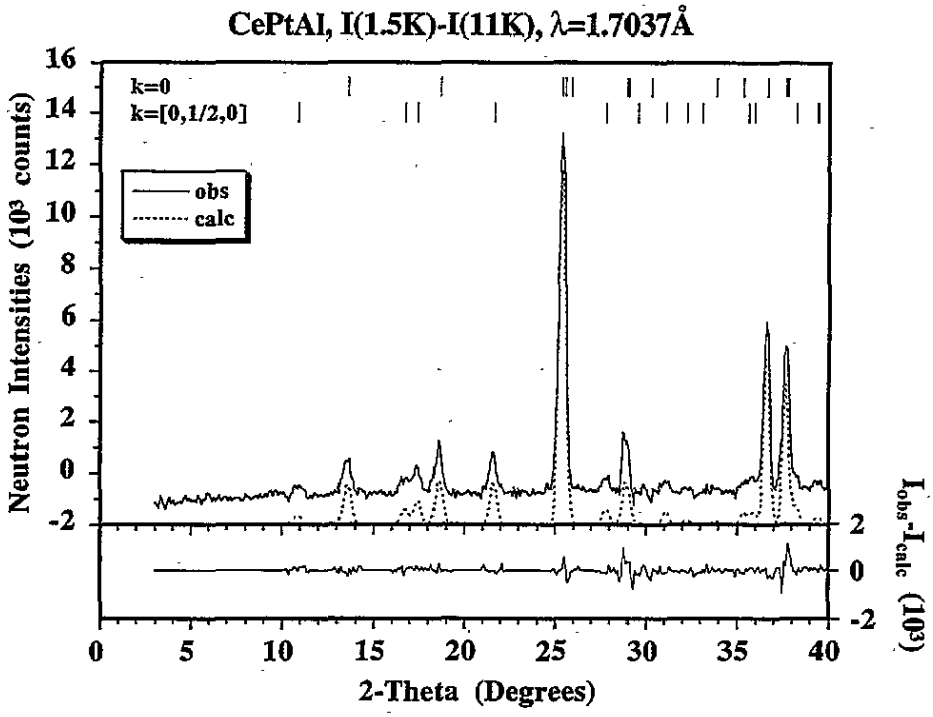

Figure 4. Rietveld fit of magnetic difference neutron diffraction pattern $I(1.5\ \mathrm{K}) - I(11\ \mathrm{K})$ of CePtAl (DMC, high-intensity mode, $\lambda = 1.7037$ Å). For clarity the curve for calculated intensities is shifted by −2000. Vertical bars on top of the figure indicate peak positions for the two contributing magnetic propagation vectors.

magnitude of the paramagnetic neutron scattering of 972 counts appears to be reasonable: it corresponds to about 13% of the total background of the spectra at 11 K, to 0.7% of the intensity maximum of the strongest nuclear Bragg peak at 11 K (14×10^4 counts) and to 7% of the intensity maximum of the strongest magnetic Bragg peak at 1.5 K (1.38×10^4 counts).

The magnetic lines of CePtAl at 1.5 K can all be indexed by the two magnetic propagation vectors $k_1 = 0$ and $k_2 = [0, 1/2, 0]$, which are both commensurate with the chemical unit cell. Magnetic reflections corresponding to k_1 are more intense and contribute 82% of the magnetic intensity observed for $2\theta \leqslant 40°$. Magnetically ordered Ce moments in CePtAl at 1.5 K are a superposition of a component due to k_1 and a component due to k_2. The full magnetic unit cell corresponds to a doubling of the chemical cell along the b axis ($b_{\mathrm{mag}} = 2b$) and contains eight magnetic Ce atoms. For Ce atoms separated by the nuclear lattice parameter b the ordered magnetic moments of the k_1 component and the k_2 component are coupled ferromagnetically and antiferromagnetically, respectively.

The magnetic structure of CePtAl at 1.5 K was determined by a standard Rietveld analysis [10] (without background fit) from the high-intensity pattern at 11 K (nuclear contribution; pattern not shown) and the difference pattern $I(1.5\ \mathrm{K}) - I(11\ \mathrm{K})$ shown in figure 4 (magnetic contribution). The calculation is based on a relativistic neutron magnetic form factor for Ce^{3+} [11]. Structural parameters of table 1 were used and kept fixed. In the fit of the 11 K pattern the scale factor and resolution parameters were refined. Here the background was used from an additional fit of the same pattern by the Wiles–Young

program. In the fit of the difference pattern $I(1.5\ \mathrm{K}) - I(11\ \mathrm{K})$ only components of the ordered magnetic moments were refined. The background was subtracted by linear interpolation from 2θ values obtained from Gaussian fits to all magnetic reflections with peak positions and widths kept fixed at the values calculated from the results of the 11 K fit. Table 2 contains the magnetic structure data for CePtAl at 1.5 K derived by Rietveld profile analysis of 13 inequivalent magnetic peaks for each of the propagation vectors k_1 and k_2. Observed and calculated magnetic integrated intensities are compared in table 3. Corresponding magnetic structures are illustrated in figure 5 (k_1 component) and in figure 6 (k_2 component).

Table 2. Magnetic structure data of CePtAl at 1.5 K derived from the difference pattern $I(1.5\ \mathrm{K}) - I(11\ \mathrm{K})$ of the DMC measurements ($\lambda = 1.7037$ Å, high-intensity mode) by Rietveld profile analysis: $b_{\mathrm{mag}} = 2b$; k_1, k_2: magnetic propagation vectors; μ_1, μ_2: magnitudes of the ordered magnetic Ce moments; α_1: angle of the ordered moment μ_1(Ce(1)) at the Ce(1) site with respect to the a axis. The agreement value concerning integrated magnetic intensities $R_{\mathrm{IM}} = \Sigma|I_{\mathrm{obs}} - I_{\mathrm{calc}}|/\Sigma I_{\mathrm{obs}}$ results to 6.0%.

				$k_1 = 0$			$k_2 = [0, 1/2, 0]$		
Atom	x/a	y/b_{mag}	z/c	$\mu_x(\mu_B)$	$\mu_y(\mu_B)$	$\mu_z(\mu_B)$	$\mu_x(\mu_B)$	$\mu_y(\mu_B)$	$\mu_z(\mu_B)$
Ce(1)	0.0305(3)	1/8	0.6782(3)	1.35(4)	0	−0.36(4)	0.55(4)	0	−0.19(3)
Ce(2)	0.4695	3/8	0.1782	1.35	0	0.36	−0.55	0	−0.19
Ce(3)	0.9695	3/8	0.3218	1.35	0	−0.36	0.55	0	−0.19
Ce(4)	0.5305	1/8	0.8218	1.35	0	0.36	−0.55	0	−0.19
Ce(5)	0.0305	5/8	0.6782	1.35	0	−0.36	−0.55	0	0.19
Ce(6)	0.4695	7/8	0.1782	1.35	0	0.36	0.55	0	0.19
Ce(7)	0.9695	7/8	0.3218	1.35	0	−0.36	−0.55	0	0.19
Ce(8)	0.5305	5/8	0.8218	1.35	0	0.36	0.55	0	0.19
				$\mu_1 = 1.40(5)\mu_B$			$\mu_2 = 0.58(5)\mu_B$		
				$\alpha_1 = -15° \pm 2°$			$\alpha_2 = -19° \pm 4°$		

We now proceed to explain the determination of the magnetic structure (results of table 2) in more detail. For the case of space group *Pnma* with Ce atoms on site (4c) and magnetic propagation vector $k_1 = 0$, the symmetry analysis of possible magnetic structures by group theory [12] yields eight one-dimensional irreducible representations Γ_i ($i = 1, \ldots, 8$), which are defined in table 4. A selective refinement of only magnetic peaks corresponding to k_1 yields the best fit for the representation Γ_2 (Shubnikov space group $Pnm'a'$) with magnetic moment configurations $F_x = 1.35(4)\mu_B$ and $C_z = -0.36(4)\mu_B$ (result of table 2) and an excellent agreement value $R_{\mathrm{IM}} = 3.7\%$ (table 3). Refinements for all other seven representations give bad agreement values $R_{\mathrm{IM}} > 40\%$, mainly due to disagreement with the intense magnetic line observed at $2\theta = 25.4°$ in figure 4. The Ce ions occupy the special positions (4c) with symmetry (.*m*.) in *Pnma*. In $Pnm'a'$ the symmetry of the site (4c) changes to an antimirror plane (.*m*'.), with the result that the magnetic moments may have components along a and c axes only. The propagation vector k_1 gives rise to a magnitude of the ordered Ce moments of $\mu_1 = 1.40(5)\mu_B$. At the Ce(1) site the angle of the ordered magnetic moment μ_1(Ce(1)) with respect to the a axis amounts to $\alpha_1 = -15° \pm 2°$. Within the experimental error the value $-\alpha_1$ turns out to be equal to α_N (see figure 3), which implies that at all Ce sites the ordered moments μ_1 are oriented parallel or antiparallel to directions determined by Ce–Ce second-nearest neighbours (e.g. Ce(1) and Ce(4)). The magnetic moment arrangement of the k_1 component is plotted in figure 5. Along the Ce–Ce nearest-neighbour chains, ordered

Table 3. Comparison of observed and calculated magnetic integrated neutron intensities of CePtAl at 1.5 K. The Bragg peaks are indexed with respect to the chemical unit cell. Estimated standard deviations corresponding to counting statistics are given in parentheses. The agreement values $R_{IM} = \Sigma|I_{obs} - I_{calc}|/\Sigma I_{obs}$ result to 3.7% (k_1) and 15.9% (k_2).

(*a*) Magnetic propagation vector: $k_1 = 0$

h	k	l	$2\theta_{calc}$ (deg)	I_{obs}	(Δ)	I_{calc}
1	0	0	13.59	8008	(160)	8152
1	0	1	18.63	8880	(158)	8554
0	1	1	25.38	52420	(232)	52588
0	0	2	25.52	12017	(72)	12323
1	1	0	25.86	386	(70)	156
1	1	1	28.90	5924	(112)	5516
1	0	2	29.02	1918	(42)	2068
2	0	1	30.27	0	(20)	94
0	1	2	33.87	646	(114)	606
2	1	0	35.32	1258	(98)	1668
1	1	2	36.65	26680	(196)	27712
2	1	1	37.67	19192	(148)	17848
2	0	2	37.76	5938	(46)	5218

(*b*) Magnetic propagation vector: $k_2 = [0, 1/2, 0]$

h	k	l	$2\theta_{calc}$ (deg)	I_{obs}	(Δ)	I_{calc}
0	1/2	0	10.91	2793	(173)	1965
0	1/2	1	16.76	3288	(120)	3026
1	1/2	0	17.45	5485	(125)	4677
1	1/2	1	21.63	7872	(158)	7602
0	1/2	2	27.82	2372	(128)	2700
2	1/2	0	29.54	94	(80)	470
1	1/2	2	31.08	1920	(124)	2246
2	1/2	1	32.26	206	(118)	844
0	3/2	0	33.10	0	(24)	180
0	3/2	1	35.38	714	(320)	678
1	3/2	0	35.93	2342	(83)	2038
1	3/2	1	38.25	3082	(110)	2982
2	1/2	2	39.42	1966	(130)	1300

moments are coupled ferromagnetically. Along the Ce–Ce second-nearest neighbour chains, ordered moments exhibit a ferromagnetic coupling (F sequence) along the a axis (parallel to the chain direction) and an antiferromagnetic coupling (with C sequence) along the c axis (perpendicular to the chain direction). Different symmetries of the irreducible representations Γ_i ($i = 1, \ldots, 8$) yield different sets of forbidden magnetic reflections. The extinctions in Γ_2 are: (0,1,1) at $2\theta = 12.7°$ ($\lambda = 1.7037$ Å), (0,1,0) at 21.9°, (2,0,0) at 27.3° and (0,0,3) at 38.7°. The experiment (figure 4), which is especially sensitive to the peak at 12.7°, gives no evidence for a violation of the symmetry corresponding to the irreducible representation Γ_2. We note that, owing to the low symmetry of the (4c) site, the relative sign between F_x and C_z components is important. On the one hand, the spin configurations 1 ($F_x = \pm 1.35\mu_B$, $C_z = \mp 0.36\mu_B$), where F_x and C_z have a different sign, are equivalent (spin inversion for all ordered moments) and describe the two magnetic domains of the k_1 component. On the other hand, the spin configurations 2 ($F_x = \pm 1.35\mu_B$, $C_z = \pm 0.36\mu_B$), where F_x and C_z have the same sign, are inequivalent with configurations 1 (agreement value $R_{IM} = 3.7\%$ and 14.5% for configurations 1 and 2, respectively).

The magnetic propagation vector $k_2 = [0, 1/2, 0]$ implies spin inversion after a

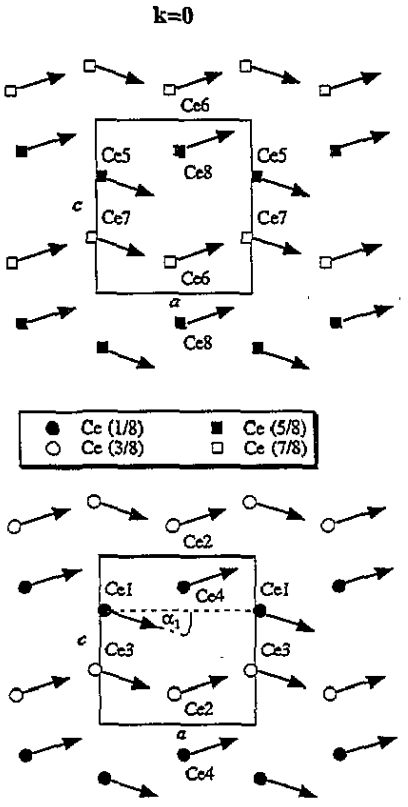

Figure 5. Magnetic moment arrangement of the component $k_1 = 0$ of the magnetic structure of CePtAl at 1.5 K plotted as a view onto (0, 1, 0) planes. The heights of the Ce atoms in units (y/b_{mag}) are indicated by numbers in parentheses in the legend. Pt and Al positions are not included in the plot.

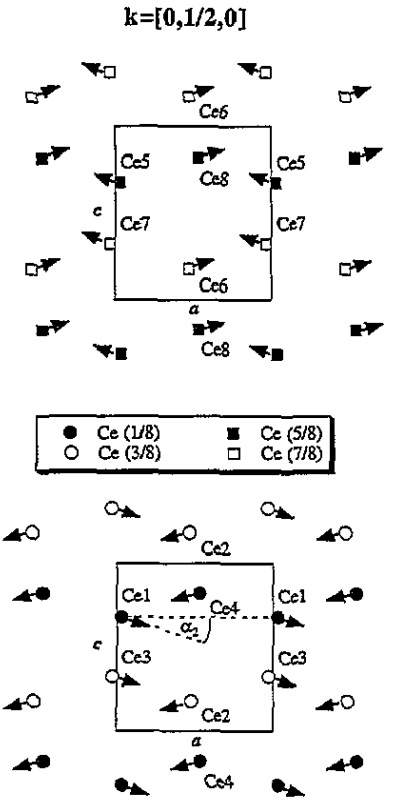

Figure 6. Magnetic moment arrangement of the component $k_2 = [0, 1/2, 0]$ of the magnetic structure of CePtAl at 1.5 K plotted as a view onto (0, 1, 0) planes. The heights of the Ce atoms in units (y/b_{mag}) are indicated by numbers in parentheses in the legend. Pt and Al positions are not included in the plot.

translation along the nuclear lattice constant b (antitranslation). We must determine the components of the ordered moments (μ_x, μ_y and μ_z) for the atoms Ce(1), Ce(2), Ce(3) and Ce(4) only. For magnetic structures with $k_2 = [0, 1/2, 0]$ group theory [12] yields two two-dimensional irreducible representations Γ_{1,k_2} and Γ_{2,k_2}, which are defined in table 4. Magnetic moment configurations F and A as well as C and G are 'partners' with the physical meaning that they provide an equivalent description (in coordinate systems with a different choice of origin) of the same physical reality. The equivalence of the two 'partners' is illustrated in figure 3 of [12] for the case of a magnetic structure different from CePtAl. We chose to work with F and C sequences and performed a selective refinement of only magnetic peaks corresponding to k_2. Representations Γ_{1,k_2} and Γ_{2,k_2} contain magnetic structures with ordered moments oriented perpendicular and parallel, respectively, to the propagation vector k_2. For the symmetry of Γ_{2,k_2} the magnetic reflection $(0, 1/2, 0)$ at $2\theta = 10.9°$ ($\lambda = 1.7037$ Å) is forbidden. This is in disagreement with the weak magnetic intensity observed in the experiment (see figure 4). Refinements of magnetic structures within Γ_{2,k_2} yield agreement values $R_{IM} \geqslant 36.6\%$. Magnetic structures of Γ_{1,k_2} have only components μ_x and μ_z. Configurations (F_x, F_z) and (C_x, C_z) give rise

Table 4. Group-theory results for magnetic configurations in case of *Pnma* and sites (4c). There are eight one-dimensional irreducible representations Γ_i $(i = 1, \ldots, 8)$ for $k_1 = 0$, and two two-dimensional irreducible representations Γ_{i,k_2} $(i = 1, 2)$ for $k_2 = [0, 1/2, 0]$.

(*a*) Configurations

(4c)				Magnetic moment configurations			
positions	x/a	y/b	z/c	F	C	A	G
(1)	x	1/4	z	+	+	+	+
(2)	$\bar{x} + 1/2$	3/4	$z + 1/2$	+	−	−	+
(3)	$\bar{x}$	3/4	$\bar{z}$	+	+	−	−
(4)	$x + 1/2$	1/4	$\bar{z} + 1/2$	+	−	+	−

(*b*) Magnetic propagation vector $k_1 = 0$

	Axial vectors			
Representation	x	y	z	Magnetic group
$\Gamma_1 = \Gamma_{1g}$	.	C	.	$Pnma$
$\Gamma_2 = \Gamma_{2g}$	F	.	C	$Pnm'a'$
$\Gamma_3 = \Gamma_{3g}$	C	.	F	$Pn'm'a$
$\Gamma_4 = \Gamma_{4g}$	.	F	.	$Pn'ma'$
$\Gamma_5 = \Gamma_{1u}$	A	.	G	$Pn'm'a'$
$\Gamma_6 = \Gamma_{2u}$	.	G	.	$Pn'ma$
$\Gamma_7 = \Gamma_{3u}$	.	A	.	$Pnma'$
$\Gamma_8 = \Gamma_{4u}$	G	.	A	$Pnm'a$

(*c*) Magnetic propagation vector $k_2 = [0, 1/2, 0]$

	Axial vectors		
Representation	x	y	z
Γ_{1,k_2}	$F(A), C(G)$	.	$F(A), C(G)$
Γ_{2,k_2}	.	$F(A), C(G)$	.

to forbidden reflections $(1, 1/2, 0)$ and $(0, 1/2, 0)$, respectively, which disagree with the experiment (figure 4). Refinements of magnetic structures with configurations (F_x, C_z) yield agreement values $R_{IM} \geqslant 35.9\%$. The best fit was obtained for $C_x = 0.55(4)\mu_B$ and $F_z = -0.19(3)\mu_B$ (result of table 2) with a fair agreement value of $R_{IM} = 15.9\%$ (table 3). Compared to the k_1 component, for k_2 weaker magnetic intensities yield a higher value of R_{IM}. The propagation vector k_2 gives rise to a magnitude of the ordered Ce moments of $\mu_2 = 0.58(5)\mu_B$. At the Ce(1) site the angle of the ordered moment μ_2(Ce(1)) with respect to the a axis amounts to $\alpha_2 = -19° \pm 4°$. Within experimental error α_2 turns out to be equal to α_1, which implies that at all Ce sites the ordered moments μ_2 are oriented parallel or antiparallel to μ_1. The magnetic moment arrangement of the k_2 component is plotted in figure 6. We note that there exists a group of additional magnetic configurations for the k_2 component with calculated neutron intensities equal to the configuration given in table 2, but with a lower symmetry with respect to the angles between μ_1 and μ_2. Examples are: $(C_x = 0.55(4)\mu_B, F_z = 0.19(3)\mu_B)$ or $(C_x = 0.55(4)\mu_B, A_z = \pm 0.19(3)\mu_B)$.

Figure 7 illustrates the result of refinements of both components k_1 and k_2 of the magnetic structure of CePtAl ($\mu_1 = (F_x, 0, C_z), \mu_2 = (C_x, 0, F_z)$) as a function of the angle α with the constraint $\alpha = \alpha_1 = \alpha_2$. The agreement value R_{IM} exhibits a well defined minimum of $R_{IM} = 6.1\%$ at $\alpha = -15°$.

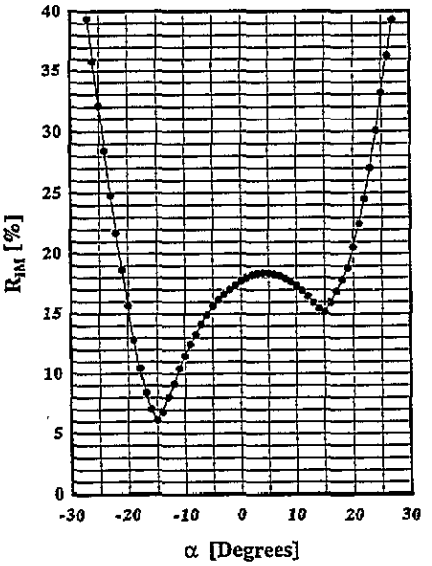

Figure 7. Agreement value R_{IM} of observed and calculated magnetic intensities of CePtAl at 1.5 K (see text) as a function of the angle α of the magnetic moment μ(Ce(1)) at the Ce(1) site with respect to the a axis. The minimum at $\alpha = -15°$ corresponds to $R_{IM} = 6.1\%$.

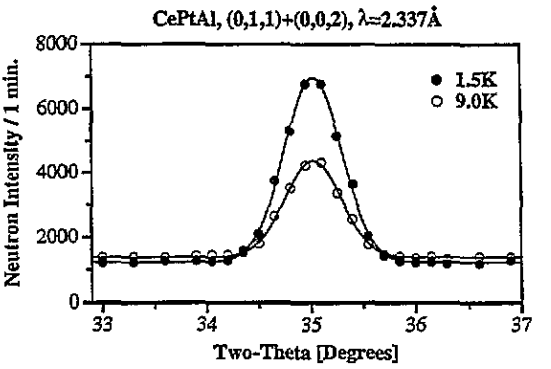

Figure 8. 2θ scans through the unresolved peaks (0,1,1) and (0,0,2) of CePtAl measured at 1.5 K (nuclear and magnetic intensities) and at 9.0 K (only nuclear intensity).

3.4. Temperature dependence of magnetic Bragg peaks

To collect information about the nature of magnetic phase transitions T_1, T_2 and T_3 of CePtAl, the temperature dependence of powder neutron intensities of selected magnetic peaks was studied between 1.5 and 11 K.

For the propagation vector $k_1 = 0$ magnetic intensity is observed below the second-order phase transition at $T_1 = 5.9$ K. The ordered moments (table 2) corresponds to $\mu_1 = (F_x, 0, C_z)$ with a temperature-independent value for the angle α_1. Figure 8 displays 2θ scans through the unresolved peaks (0,1,1) and (0,0,2) at 1.5 K (nuclear and magnetic intensities) and at 9.0 K (only nuclear intensity). The peak of figure 8 shows the strongest magnetic intensity, which is of pure ferromagnetic origin with no contribution from the C_z sequence. The temperature dependence of magnetic intensity, plotted in figure 9, describes a second-order phase transition with slight anomalies near and above $T_2 = 4.3$ K. The (1,0,0) reflection is forbidden by the symmetry of the nuclear structure (space group $Pnma$) and only the C_z sequence contributes to the observed weak magnetic intensity (see figure 10) with I_{max} corresponding to only about twice the change of background between the paramagnetic and magnetically ordered phase of CePtAl. Within the precision of the measurement the ratio of magnetic intensities between the peaks shown in figures 8 and 10 is temperature-independent. The reflection (1,0,1) was studied to search for a possible temperature-dependent change of the relative sign between F_x and C_z sequences with a negative result.

For the propagation vector $k_2 = [0, 1/2, 0]$ magnetic intensity is observed below the first-order phase transition at $T_2 = 4.3$ K. The accuracy of the experiments was limited by the considerable weakness of magnetic peaks. The intensity of the strongest magnetic reflection (1,1/2,1), displayed in figure 11, is comparable to the weak magnetic peak (1,0,0)

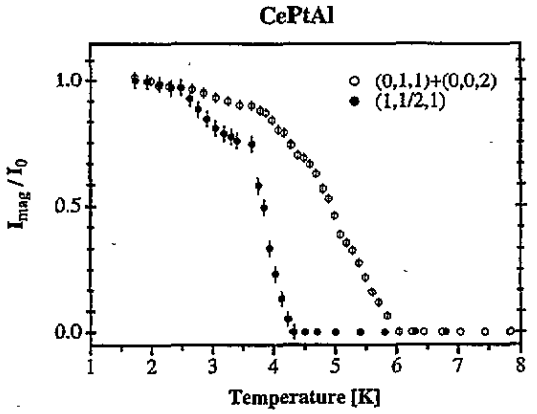

Figure 9. Temperature dependences of magnetic neutron intensities of the unresolved peaks (0,1,1) and (0,0,2) and of the reflection (1,1/2,1) measured for decreasing temperature.

shown in figure 10. The temperature dependence of magnetic intensity of the (1,1/2,1) peak is plotted in figure 9. The large width ($\Delta T_2 \simeq 0.6$ K) of the first-order phase transition at $T_2 = 4.3$ K is due to the powder measurement. In a single-crystal experiment a much sharper phase transition can be expected. At the first-order phase transition $T_3 = 2.2$ K, no change of propagation vector occurs, but an increase of magnetic intensity is observed for the (1,1/2,1) peak around $T_3 \simeq 2.5$ K (figure 9). Magnetic intensities of all peaks (0,1/2,0), (1,1/2,0), (0,1/2,1) and (1,1/2,1) are stronger at 1.5 K than at 3.6 K.

Between $T_1 = 5.9$ K and $T_2 = 4.3$ K the existence of an additional incommensurate propagation vector $k_3 = [0, 0.463(8), 0]$ was confirmed by detecting the magnetic peaks (0,0.54,0), (0,0.54,1) and (1,0.463,1). Measurements of the magnetic reflection (1,0.463,1) at 4.73 K, 5.0 K (see figure 11) and 5.5 K revealed no temperature dependence of the peak position. However, the width of the incommensurate peak (1,0.463,1) is broader than the width of the commensurate magnetic peak (1,1/2,1). The latter corresponds to the instrumental resolution. In CePtAl the correlation length for the incommensurate magnetic structure is smaller than for the commensurate magnetic structure.

For CePtAl with magnetic phase transitions at $T_1 = 5.9$ K (second order), $T_2 = 4.3$ K (first order) and $T_3 = 2.2$ K (first order), we find the following magnetic propagation vectors:

$T > T_1$	no magnetic Bragg peak		
$T_1 \geqslant T \geqslant T_2$	$k_1 = 0$	and	$k_3 = [0, 0.463(8), 0]$
$T_2 \geqslant T$	$k_1 = 0$	and	$k_2 = [0, 1/2, 0]$.

4. Discussion

The case of a nuclear structure with orthorhombic space group *Pnma* and magnetic atoms on site (4c) is frequently encountered. As an illustrative example we quote the recently investigated compound K_2UBr_5 [13, 14]. In K_2UBr_5 the magnetic U^{3+} atoms form chains parallel to the *b* axis, which are well separated from each other. The intrachain U–U distance of 4.78 Å is much smaller than the shortest interchain U–U distance of 7.18 Å. Magnetic

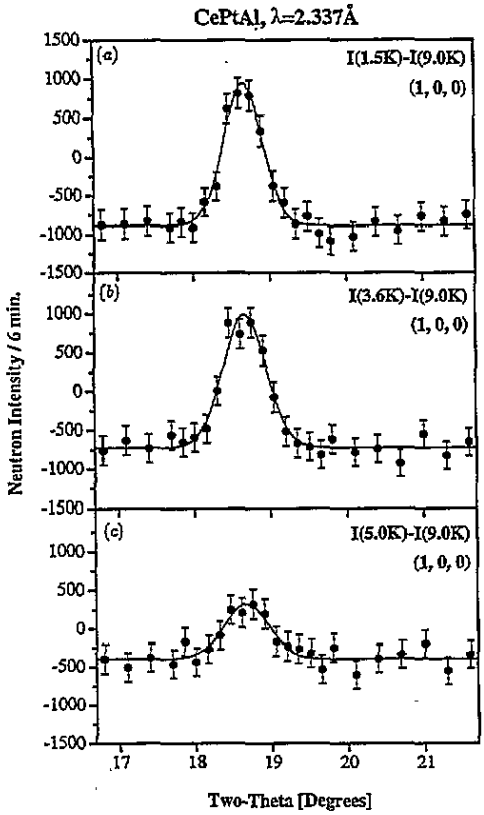

Figure 10. Magnetic neutron intensity of the (1,0,0) peak of CePtAl at (*a*) 1.5 K, (*b*) 3.6 K and (*c*) 5.0 K.

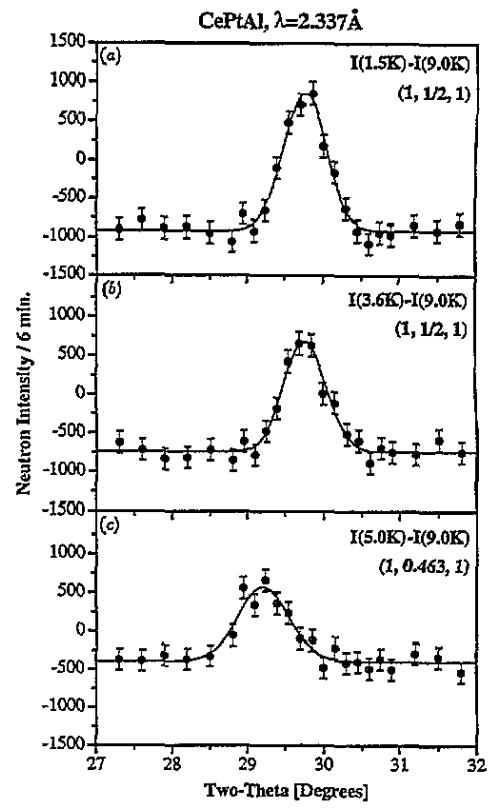

Figure 11. Magnetic neutron intensity of the (1,1/2,1) reflection of CePtAl at (*a*) 1.5 K and (*b*) 3.6 K. (*c*) An incommensurate magnetic peak (1,0.463(8),1) is observed at 5.0 K.

exchange interactions in K_2UBr_5 are highly anisotropic, with the strongest coupling parallel to the chain direction. Three-dimensional, predominantly antiferromagnetic long-range order occurs at $T_N = 2.8$ K (propagation vector $k = 0$, representation Γ_5 with $A_x = 1.66(4)\mu_B$ and $G_z = 1.60(4)\mu_B$). Above T_N a peak in the magnetic susceptibility of K_2UBr_5 around 10 K indicates local one-dimensional magnetic ordering along the U chains. From the magnetic entropy, $R \ln 2$, of the crystalline electric field ground-state doublet about 90% is released above the phase transition to three-dimensional magnetic ordering at T_N. The magnetic part of the specific heat, c_{mag}, of K_2UBr_5 consists of a sharp anomaly at T_N and a broad peak above T_N, which could be nicely reproduced by a calculation based on a highly anisotropic two-dimensional Ising model.

Unlike the case of K_2UBr_5, where the magnetic U atoms form well separated chains, in CePtAl the Ce–Ce distances for nearest neighbours (3.56 Å) and second-nearest neighbours (3.77 Å) are not very different. The result is a network of Ce–Ce nearest-neighbour chains (parallel to the *b* axis) and Ce–Ce second-nearest-neighbour chains (along the *a* axis) with competing anisotropic magnetic exchange interactions. They appear to provide the inherent conflict built into the chemical structure, which is necessary for the occurrence of the unusually complex magnetic structures found in CePtAl. Low-dimensional magnetic ordering, like in K_2UBr_5, is not expected for CePtAl, where only about 28% of the

magnetic entropy $R \ln 2$ of the ground-state doublet is released in magnetic correlations above $T_1 = 5.9$ K.

A refinement of the magnetic structure of CePtAl at 1.5 K from the zero-field powder neutron diffraction pattern of figure 4 yields the k_1 and k_2 components of the magnetically ordered moments (result of table 2) but not the nature of coupling between the two Fourier components. For the predominantly ferromagnetic k_1 component strong observed magnetic intensities allowed an accurate determination of the magnetic structure, which is in agreement with the magnetization experiment. The large ferromagnetic component, $F_x = 1.35(4)\mu_B$ at 1.5 K and $F_x = 0.9(1)\mu_B$ at 5.0 K (from table 2 and figure 9), points along the a direction, the magnetic easy axis of CePtAl. The magnetization curve m_a of CePtAl at 5.0 K [5] yielded a spontaneous magnetic moment of $1.0\mu_B$ and an extrapolated ferromagnetic saturation moment of $1.35\mu_B$. For the antiferromagnetic k_2 component the accuracy of the structure determination is limited by the weakness of observed magnetic neutron peaks.

In the simplest case of a single-k_1/single-k_2 configuration in CePtAl the magnetic structure is a superposition of the two components shown in figures 5 and 6. Then the results of table 2 imply that the magnitude of the ordered magnetic moment $|\mu| = |\mu_1 + \mu_2|$ is not constant (modulated) and takes the two values $\mu_1 + \mu_2 = 1.98(10)\mu_B$ at Ce(1), Ce(3), Ce(6) and Ce(8) and $\mu_1 - \mu_2 = 0.82(10)\mu_B$ at Ce(2), Ce(4), Ce(5) and Ce($\bar{7}$). The magnetic moment magnitude of a single-k_1/single-k_2 structure is constant if the k_2 component μ_2 is perpendicular to the k_1 component μ_1 at the positions of all Ce atoms. A systematic investigation of such magnetic structures yielded agreement values R_{IM} of the k_2 component, which are at least 2.3 times worse than for the result summarized in table 2. Moreover, based on the results of the present experiment the construction of a magnetic structure of CePtAl with *exactly* constant spin magnitudes is not possible, even for the case of a general single-k_1/multi-k_2 configuration.

The question of whether and how the magnitudes of the ordered moments in CePtAl are modulated depends on the yet unknown kind of coupling of the k_1 and k_2 components, and in addition on the accuracy of the structure determination for the weak intensities of the k_2 component. For an answer the results of future single-crystal experiments of magnetic field or pressure dependence of magnetic neutron intensities of CePtAl must be awaited. We mention the rule that antiferromagnetic structures with ordered moments that vary not too much in magnitude with position are favoured, which has been suggested [15] based on results of reinvestigations of the modulated magnetic structures of Nd [16] and $CeAl_2$ [17] and a consideration of the free energy [15].

In CePtAl the possible magnetic moment modulations (described by the k_2 and k_3 components) are incommensurate between $T_1 = 5.9$ K and $T_2 = 4.3$ K and commensurate below T_2. The first-order phase transition at $T_3 = 2.2$ K may be due to a change of coupling between the k_1 and k_2 components. The relative sizes of the steps in the electrical resistivity (figure 1) provide some additional information about the phase transitions T_2 and T_3. The dominant change in the magnetic structure happens in the components parallel to a and b axes (the two chain directions) at T_2 and in the component parallel to the c axis at T_3.

The present bulk physical measurements on single crystals (electrical resistivity, specific heat, magnetic susceptibility) and powder neutron diffraction results provide the first important information on the complex magnetic ordering phenomena of the intermetallic rare-earth compound CePtAl. In particular, the magnetic ground state corresponding to the two propagation vectors $k_1 = 0$ and $k_2 = [0, 1/2, 0]$ has been established. For more detailed investigations—in particular of the temperature dependence of the incommensurate

magnetic ordering—neutron single-crystal experiments will be needed. We hope to provide such additional results at a later date.

Acknowledgments

We gratefully acknowledge financial support from the Special Coordination Fund of the Science and Technology Agency of Japan and a Grant-in-Aid from the Ministry of Education, Science and Culture of Japan. Experiments in Switzerland were financially supported by the Swiss National Science Foundation.

References

[1] Maletta H and Sechovsky V 1994 *J. Alloys Compounds* **207** 254
[2] Hulliger F 1993 *J. Alloys Compounds* **196** 225
[3] Xue B and Schwer H 1994 *J. Alloys Compounds* **204** L25
[4] Schank C, Jährling F, Luo L, Grauel A, Wassilew C, Borth R, Olesch G, Bredl C D, Geibel C and Steglich F 1994 *J. Alloys Compounds* **207** 329
[5] Kitazawa H 1994 unpublished results
[6] Toraya H 1986 *J. Appl. Crystallogr.* **19** 440
[7] Schefer J, Fischer P, Heer H, Isacson A, Koch M and Thut R 1990 *Nucl. Instrum. Methods Phys. Res.* A **288** 477
[8] Wiles D B and Young R A 1981 *J. Appl. Crystallogr.* **14** 149
[9] Sears V F 1992 *Neutron News* **3** 26
[10] Rietveld H M 1969 *J. Appl. Crystallogr.* **2** 65
Hewat A W 1973 *UKAEA Harwell Report* R7350
[11] Freeman A J and Desclaux J P 1979 *J. Magn. Magn. Mater.* **12** 11
[12] Bertaut E F 1968 *Acta Crystallogr.* A **24** 217
[13] Krämer K, Keller L, Fischer P, Jung B, Edelstein N N, Güdel H U and Meyer G 1993 *J. Solid State Chem.* **103** 152
[14] Keller L, Furrer A, Fischer P, Allenspach P, Krämer K, Güdel H U, Dönni A and Suzuki T 1995 *Phys. Rev.* B at press
[15] Forgan E M 1992 *J. Magn. Magn. Mater.* **104–107** 1485
[16] McEwen K A, Forgan E M, Stanley H B, Bouillot J and Fort D 1985 *Physica* B **130** 360
McEwen K A and Walker M B 1986 *Phys. Rev.* B **34** 1781
[17] Forgan E M, Rainford B D, Lee S L, Abell J S and Bi Y 1990 *J. Phys.: Condens. Matter* **2** 10211